PILLARED SODIUM MANGANESE OXIDE AS A CATHODE MATERIAL FOR SODIUM-ION BATTERIES

BY

DANIEL G. MUSCATO

BS, Binghamton University, 2024

THESIS

Submitted in partial fulfillment of the requirements for
the degree of Master of Science in Materials Science and Engineering
in the Graduate School of
Binghamton University
State University of New York
2025

Submitted in partial fulfillment of the requirements for
the degree of Master of Science in Materials Science and Engineering
in the Graduate School of
Binghamton University
State University of New York
2025

December 8, 2025

Hao Liu, Chair and Faculty Advisor
Department of Chemistry, Binghamton University

Manuel Smeu, Member
Department of Physics, Binghamton University

Brent Melot, Member
Department of Chemistry, Binghamton University

Abstract

Sodium-ion batteries offer an alternative solution to the current lithium market. Layered transition-metal oxides, such as P2-$Na_{2/3}MnO_2$, serve as highly tunable, easy-to-synthesize cathode materials. While sodium-ion cathodes have the potential to deliver high capacities, they suffer from phase changes that lead to structural collapse and long-term capacity fade. This material exhibits P2→OP4 phase changes at high voltages and P2→P'2 at low voltages. Recent research on pillaring aims to incorporate cations into the structure of Na-LTMOs to suppress detrimental phase transitions in sodium cathode materials. Previous studies have shown an improvement in structural stability through pillaring, by doping with a larger alkali ion than Na^+, such as K^+, which widens the interlayer spacing and improves sodium diffusion. However, studies involving the substitution of similarly sized ions, such as Ca^{2+}, have not been reported for the P2-$Na_{2/3}MnO_2$ material. This research project aims to explore the pillaring effects of Ca on the mitigation of the capacity degradation of the P2-$Na_{0.67-2y}Ca_yMnO_2$ material. In this work, I have identified various synthesis parameters relevant for the formation of pure P2-$Na_{2/3}MnO_2$ and have reported a refined synthesis for the Ca-ion exchange across $0 \leq y \leq 0.15$. Powder X-ray diffraction (XRD) techniques are used to characterize the crystal structure of the P2 and Ca-pillared materials, along with operando XRD to investigate the structural evolution during charge/discharging. Galvanostatic electrochemical tests are used to observe the long-term cycling performance of the y = 0.00, 0.05, 0.10, and 0.15 materials. The substituted y = 0.05 material exhibits suppressed phase changes in comparison to the y = 0.00 sample, including outperforming its capacity and retention after just 40 cycles, reflecting the effects of successful pillaring.

I declare that no generative artificial intelligence (AI) tools or services were used in the research, writing, analysis, or any other aspect of this thesis.

Table of Contents

List of Tables

List of Figures

List of Abbreviations

AQ	**A**nneal-**Q**uenched
SIB	**S**odium-**I**on **B**attery
LIB	**L**ithium-**I**on **B**attery
LTMO	**L**ayered **T**ransition **M**etal **O**xide
NMO	**N**$a_{2/3}$**M**n**O**$_2$
TM	**T**ransition **M**etal
TMO	**T**ransition **M**etal **O**xide
XRD	**X**-**R**ay **D**iffraction

Introduction

Lithium-ion batteries (LIBs) have become the staple for efficient energy storage devices, ranging from portable electronics to electric vehicles. Their wide range of uses stems from their ability to perform well under high and low voltage strain without the development of irreversible side reactions.[3] The groundwork for LIBs and intercalation chemistry was laid out in the early 1970s by Whittingham, who worked on the Li_xTiS_2 system.[4] This preliminary work employed a layered titanium disulfide (TiS_2) cathode paired with a lithium metal anode, where Li^+ ions were reversibly inserted into a host lattice without hindering its integrity.[5] This system only achieved a working voltage of ~2.5V, which, combined with other safety concerns, rendered this material unsuitable for widespread commercial use.[6,7] In 1980, Goodenough further advanced the field by demonstrating lithium cobalt oxide ($LiCoO_2$, LCO) as a cathode material.[8] This system offered a much higher operating voltage of ~4.2V, enabling commercial viability.[8,9] Following that advancement, Yoshino evaluated a carbon fiber for its effectiveness as an anode for the LCO system. It was found that the crystalline structure of the anode was perfect for the intercalation mechanics of the Li^+ ions.[10] The cultivation of these advancements led to the first commercialized battery in 1991 by Sony and Asahi Kasei, and the eventual recognition of the 2019 Nobel Prize in Chemistry awarded to Whittingham, Goodenough, and Yoshino.[11]

Lithium-ion technology made several advances over the next few decades, giving us high-energy density, long cycle life, and efficient energy storage devices we use every day. Despite these advantages, lithium has substantial environmental concerns and a rapidly decreasing supply. It is

estimated that with a 5% growth rate in the lithium demand, our current resources may only last another 65 years.[12–14] Three main countries (Australia, Chile, and China) account for the majority of the mining, refining, and associated infrastructure of lithium materials. This small geographical distribution raises concern for global supply chains.[14] Additionally, the most popular form of lithium mining, known as brine extraction, involves a large usage of fresh water, affecting the surrounding communities and ecosystems.[15] With this alarming rate of consumption, environmental impacts, and the selective locations for mining this rare material, researchers have begun to focus more on beyond-lithium battery technology.

A promising solution to the growing demand for energy storage is the development of sodium-based batteries. SIBs have similar intercalation mechanisms to LIBs, resulting from both elements being in the alkali metal group. These single-valence-electron ions contain high charge-to-mass ratios, which allows Na to have the second-highest energy density of the alkali metals, after Li.[16] Additionally, sodium is the fourth most abundant metal, which makes it 1180 times more abundant than lithium in the Earth's crust.[17,18] Cell components of SIBs are almost identical within the battery, along with their intercalation mechanisms.[20] As a result of its high abundance and low-cost advantages, industries have taken steps to evaluate sodium-ion cathodes for their efficiencies in small-scale electronics. SIB cathodes range in structure, including layered transition metal oxides (LTMOs), poly-anion compounds, and Prussian blue analogues.

LTMOs are among the most versatile cathode materials due to their compositional diversity, simple synthesis, and high energy density.[21] LTMOs are composed of transition metal-oxygen octahedra that are stacked with alkali metal ions (such as Na or Li) in between. The layered structure facilitates the diffusion of the alkali ions in and out of the cathode material, allowing

for this type of material to attract the attention of many sodium-ion cathode researchers.[22,23] With this structure, the ratios of transition metals, along with the charge carrier ion, can be tuned through simple synthesis adjustments, offering high theoretical capacities.[24] In most Na_xTMO materials, such as NMO, the sodium ions are found in prismatic (P) or octahedral (O) sites located between 'slabs' of transition metal oxides. The number of layers in the unit cell is denoted by a number 2-4, such as the structures shown in Figure 1. In comparison to Li-ion analogues, sodium's ionic radius is much larger (1.02 Å vs. 0.76 Å for Li^+). The widening of layers caused by Na^+ can be an advantage, as it allows for enhanced diffusion during charge-discharge cycling.[25] However, large vacancies left by the Na^+ ions during charging lead to weakly bonded layers, which can induce the gliding or shifting during cycling and significantly reduce the long-term capacity of these batteries. Shifting/gliding is a result of a lower energy geometry being more favorable at lower interlayer spacing, causing, for example, a P2 structure to phase change to an O2 structure during desodiation.[18] Figure 1 illustrates the typical phases of Na_xTMO materials along with the probable phase transitions.[26]

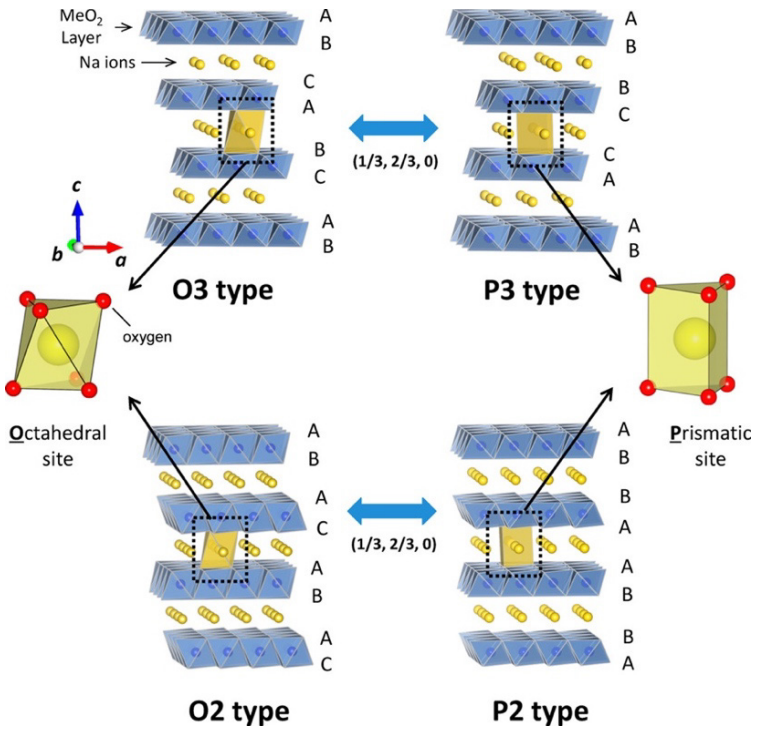

Figure 1. Depiction of possible crystal lattice structures available to Na_xTMO_2. Layered stacking of edge-sharing TMO_6 octahedra and reversible phase transitions are shown.[1]

Capacity fade stemming from phase instability during cycling is among the greatest issues for LTMO materials. Due to the larger size of Na^+, Na_xTMO materials have more freedom to transition in and out of rigid structures, leading to semi-irreversible phase changes.[27] When the structure shifted to a lower energy state, it can decrease the *c* lattice parameter, which then impedes the re-insertion of Na^+ ions and effectively collapses the diffusion pathways in the cathode material. One way to mitigate this effect is to partially replace the alkali ion with other cations to stabilize the TMO layers. This process is known as cation pillaring.

Cation Pillaring

Along with transition-metal site substitution, cation pillaring of the alkali ion site can have structural benefits as well. Pillaring refers to the act of inserting foreign cations into the interlayer between the TMO slabs, effectively acting as pillars in a building, keeping the ceiling

and floor spaced far enough for objects to travel freely between, in this case, Na^+ ions diffusing through the TMO slabs. These pillars can anchor the slabs within the material and can aid in maintaining the desired phase of the cathode during cycling. One approach to pillaring has been to use a larger ion, such as K^+, for the substitution of Na^+, which allows for an expansion of the TM-TM interlayer distance.[28–30] This interlayer expansion has been observed to improve the electrochemical performance by favoring the kinetics of interlayer diffusion of the Na^+ ions. Another approach is to substitute a similarly sized ion, such as Ca^{2+}. This method can improve the electrochemical performance and ambient stability of the cathode material.[31,32] There are certainly trade-offs to consider when using cation pillaring in a battery material. Since these pillaring cations often occupy redox-inactive sites, they reduce the theoretical capacity of the material due to the ions not participating in the charge migration. Additionally, excessive cation substitution can impede Na^+ diffusion by blocking intercalation pathways, underscoring the importance of the substitution ratio.

Sodium Manganese Oxide (NMO)

The study of NMO draws the attention of many battery chemists for its wide variety of polymorphs, accessible by alteration of sodium content and synthesis conditions.[33] The layered Na_xMnO_2 structure was first investigated by Parant *et al.* in 1971 and continued in 1981 by Delmas, revealing that the Mn-O framework yields the capability to accommodate sodium in multiple different coordination environments.[34,35] Typically, Na_xMnO_2 can be categorized into two-dimensional (2D) and three-dimensional (3D) types of structures. This work only focuses on the 2D type structure, where $x>0.5$.[36] Three phases of the 2D-NMO material have been identified: hexagonal P2-$Na_{2/3}MnO_2$ (*$P6_3/mmc$* space group), monoclinic O'3 α-$NaMnO_2$ (*C2/m*

space group), and orthorhombic P'2-$NaMnO_2$ (*Cmcm* space group).[24,37] The structures of the α-NMO and P'2-NMO polymorphs are shown in Figure 2. Synthesis of a specific polymorph is typically achieved by tuning the calcination temperature and cooling protocol. The orthorhombic P'2 polymorph is reported to be a high-temperature material, existing at temperatures above 1000°C.[36,38] Additionally, O'3 α-$NaMnO_2$ has been reported to be stable at temperatures between 600°C and 850°C.[39]

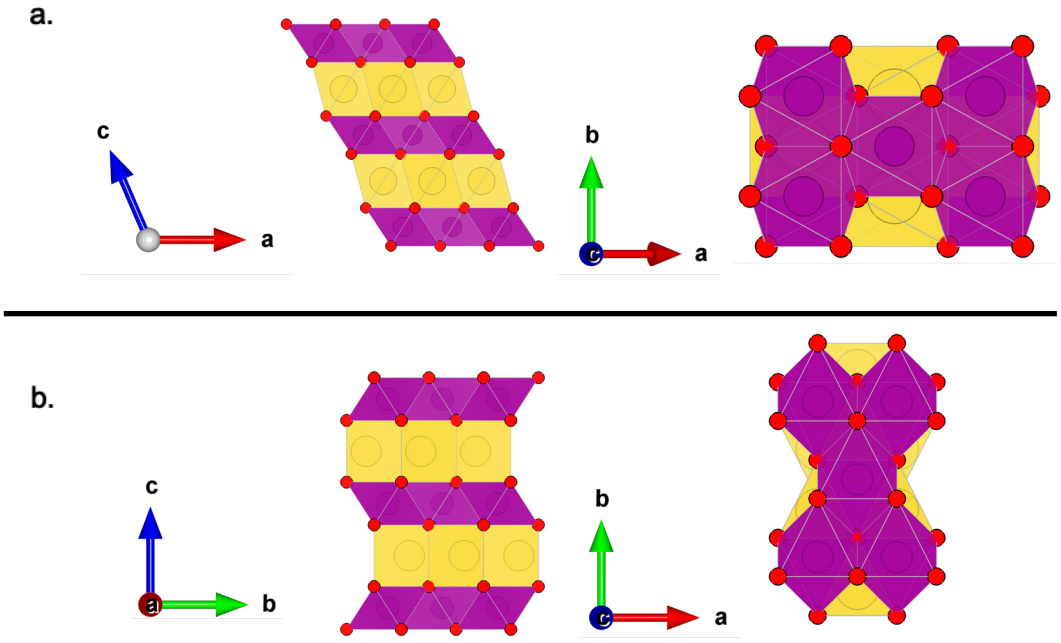

Figure 2. Structures of (a) α and (b) P'2 polymorphs of $NaMnO_2$ (yellow = sodium atoms; red = oxygen atoms; purple = MnO_6 octahedral slabs).

For this study, the recent advancements of P2-$Na_{0.7}MnO_2$ in a hexagonal structure will be discussed to establish the groundwork for this research. This P2-type material exhibits the LTMO stacking sequence of ABBA, where the total prismatic sites are split between edge and face sharing with the MnO_6 slabs.[40] Figure 3 illustrates the structure of a P2-$NaMnO_2$, including the locations of the edge and face-sharing Na^+ sites in the lattice structure.[23]

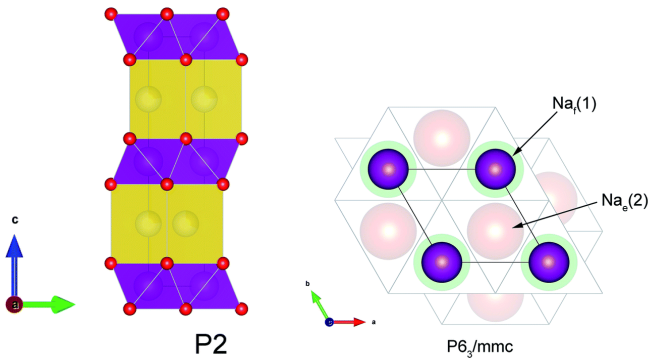

Figure 3. P2 (hexagonal *P6₃/mmc*) $NaMnO_2$ with the approximate locations of face and edge sharing prismatic sodium sites.[2]

The electrochemical reaction mechanism for NMO materials has been observed from previous operando XRD studies, which record various XRD patterns of the cathode material during a charge/discharge cycle. For P2-NMO, the transition of Mn^{3+} to Mn^{4+} is responsible for the conduction. As the cell is charged, Na^+ is removed from the interlayer sites, and Mn^{3+} is oxidized to Mn^{4+}. This Na removal is responsible for weakening the interlayer repulsion between the transition metal slabs and often leads to layer gliding and phase transitions, which can be observed by XRD characterization.[36,37] An operando study done by Kulka *et al.* on a P2-$Na_{0.706}MnO_2$ yielded evidence of a P2→OP4 transition at high charge voltages and a P2→P'2 transition during full discharge.[30] These transitions corresponded to a volume variation of 11.2%, indicating structural instability during cycling.[30] The electrochemical properties of P2-NMO have been studied extensively along with its diffusion kinetics.[23,27,38,41] In a study comparing the electrochemical performance of pure P2-NMO with P2/P'2 hybrids, Kulka *et al.* found that the pure P2-NMO topped out at 180 mAh/g within the first specific charge on discharge. However, the P2 cathode suffered capacity fade, which was attributed to the gliding of the MnO_6 slabs and the thermodynamic instability of the prismatic sodium sites.[2] Furthermore, Kumakura *et al.* reported an energy density of 490 Wh $(kg\text{-}oxide)^{-1}$ with an initial reversible capacity of 198

mAh/g.[38] Nonetheless, capacity degradation is unavoidable and falls below 80% capacity retention after only 25 cycles when cycled between 1.5-4.4V.[38] NMO has proven itself to be a sodium-ion cathode material that can demonstrate a high specific capacity, but it falls short in long-term capacity fade.

Objective

The goal of this project is to explore the pillaring effect of Ca in the P2-$Na_{0.67-2y}Ca_yMnO_2$ cathode material. NMO is a well-studied and highly tunable sodium-ion cathode material that is made with abundant materials. Inexpensive solid-state synthesis routes allow for different polymorphs of NMO to be achieved with ease. This study aims to report an adjustable solid-state synthesis to allow easier reproducibility of the P2-NMO cathode material, in addition to a refined method for the Ca-ion exchange. Previous studies have not explored the calcium substitution of the P2-NMO material, but it has been studied with other alkali ions such as potassium.[30] Characterization techniques such as powder XRD, operando XRD, and galvanostatic charge/discharge cycles will show the effects of calcium integration on P2-NMO.

Materials and Methods

The P2-phase $Na_{2/3}MnO_2$ was synthesized using a solid-state reaction scheme. Precursor powders of $NaCH_3COO$ ≥99% from Sigma-Aldrich and MnO_2 ≥99% from Sigma-Aldrich were used without drying or purification. The powders were weighed in stoichiometric ratios, with the addition of 10% sodium to offset evaporation during heating, and ground with an Across International planetary ball mill for 12 h at 400 rpm in the presence of acetone. A batch size of 13-15 g was typical for these starting materials. The homogenized precursor mixture was dried overnight in a vacuum oven at 80°C. Once completely dry, the mixed powders were pressed into 1.5 g pellets at 150 bar for about one minute. Around 2-4 pellets were stacked in the center of an alumina crucible and heated for 2 h at 500°C, directly followed by 10h at 900°C in air using a box furnace, with a heating rate of 5°C/min and a cooling rate of 2.5°C/min. The products were transferred to an argon-filled glovebox and ground to a powder for characterization.

Calcium-Ion Exchange

Substitution of Ca for Na in NMO followed an ion-exchange reaction previously described by Yikang Jing *et al*., where a standard solid-state reaction process was used to insert calcium into the alkali layer of NMO.[31] The samples were labeled as CaX%-NMO, with X% representing the planned calcium occupancy of the interlayer before synthesis. First, a calcium nitrate hydrate ($Ca(NO_3)_2 \cdot 4H_2O$) from Sigma-Aldrich was dehydrated by heating to 250°C for 24 hours in air using a box furnace, then ground with a mortar and pestle. The anhydrous $Ca(NO_3)_2$ was

transferred to an argon-filled glovebox. In a typical synthesis, 1-3 g of powdered NMO was mixed in a mortar and pestle with anhydrous $Ca(NO_3)_2$ (10% excess Ca) at a specific stoichiometric ratio. The mixture was quickly removed from the glove box, pelletized at 150 bar for about one minute, and placed into a box furnace with the pellet centered in an alumina crucible. The material was heated to 300°C for 24 h in air at a rate of 5°C/min and allowed to cool naturally to room temperature before being transferred to a glovebox and ground into a fine powder. During the synthesis, the evolution of $NaNO_3$ occurs and needs to be washed out of the product. For washing, the powdered product was transferred out of the glovebox and into an Erlenmeyer flask filled with ~75 mL of DI water per 1g of material, and a stir bar. The product was stirred at room temperature for 10 min, followed by centrifugation and decanting of the $NaNO_3$ water mixture. After vacuum drying, the product was returned to the glovebox.

An additional annealing step was performed on the Ca5%-NMO and Ca10%-NMO samples to increase the phase miscibility between the lattice structures with and without the Ca substitution. This step was done by re-pelletizing the material and heating in a box furnace, at 5°C/min, to 500°C and holding for 2 h, followed by a quench to room temperature. This process was observed to be necessary for the formation of a single-phase product.

Characterization

Powder XRD was performed on a Bruker D8 Advance instrument using a Mo Kα source ($K\alpha_1$ = 0.7093 Å, $K\alpha_2$ = 0.7136 Å) and a LynxEye XE-T linear position-sensitive detector in 1D configuration. Data was acquired in Bragg-Brentano geometry at room temperature using zero-background sample holders. Structural refinements were carried out with TOPAS Academic

(Bruker AXS, Coelho Software), with instrumental peak broadening corrected by comparison to a LaB_6 standard, using TCHZ profile parameters and the software's LPSD instrumental model.

Cathode preparation was carried out using the slurry deposition method. An 8:1:1 ratio by weight of active material (P2-$Na_{0.67-2y}Ca_yMnO_2$), carbon black (Alfa Aesar), and poly(vinylidene fluoride) (Sigma-Aldrich) was mixed with 1-methyl-2-pyrrolidinone and spread on aluminum foil with a doctor blade. The slurry spread was dried in a vacuum oven at 80°C overnight, or until it was fully dried. A 12 mm punch was used to cut out electrode disks with a typical active mass loading of 5.5 mg/cm^2. Electrochemical testing was conducted using a standard coin cell construction. The coin cell parts were of the CR 2032 type and consisted of an anode case, a cathode case, a wave spring, and a steel disk. The electrolyte used was a solution of 1 M $NaClO_4$ in propylene carbonate with 1% fluorinated ethylene carbonate. Metallic sodium was spread onto the steel disk and used as the anode of the cells. The separator used was a glass fiber.

The galvanostatic charge/discharge test is the most popular electrochemical test for battery materials. It involves charging the cell at a constant current, expressed by a C rate, until a voltage threshold is reached. After a rest cycle with no current, the reverse current is applied until finally reaching a lower voltage threshold. The corresponding potential response versus time, or capacity, is recorded. The produced voltage *vs.* capacity plots provide key insight into the diffusion kinetics, reaction reversibility, capacity degradation, and phase changes of the cathode materials.[42] Short and long-term galvanostatic cycling of the coin cells was conducted on Landt CT3001A (Landt Instruments) cell cyclers with an operating voltage window between 1.5 and 4.4 V at room temperature. A theoretical capacity of 243 mAh/g was calculated for the P2-NMO

material, which allowed for the specific current to be influenced by the active material contained within each cell. The cycling rate was set to C/20, and data was collected in ten-second intervals.

Synchrotron XRD data were taken using beamline 28-ID-2 of the National Synchrotron Light Source II, by Brookhaven National Laboratory. Capillaries of 50 mm tall were filled with the sample and sealed using a quick-drying epoxy. In-operando XRD samples were also constructed using custom coin cells with designed cut-out windows to allow the beamline to analyze the cathode material. A wavelength of 0.1811 Å was used. Synchrotron measurements were conducted by Anthony T. Pacileo.

Results and Discussion

Synthesis Optimization

When following the procedures outlined by previous studies, a mixture of P2, α, and P'2 polymorphs of NMO is often produced. Alterations in various synthesis parameters were necessary to achieve the phase-pure product. Of these synthesis parameters, it was found that the mixing style of the precursors was of importance as much as the synthesis temperature and cooling rate. Previous attempts done with an insufficient amount of mixing and not in the presence of acetone yielded phase impurities in the product. Figure 4 shows the X-ray diffraction patterns measured for two samples prepared with the same calcination parameter but different mixing protocols: mixing precursors ($NaCH_3COO$ and MnO_2) for a total of 2 hours at 600 rpm without acetone in a planetary ball mill resulted in a secondary monoclinic α phase, whereas mixing for a total of 12 hours at 400 rpm in acetone yielded the pure P2 phase. Solvent-assisted ball milling can reduce the particle size of precursor powders and allow for a more homogenous mixture, yet it requires an additional drying step before pelletizing.[43] In this study, it has been found that a more homogeneous mixture is necessary to form the pure P2 phase.

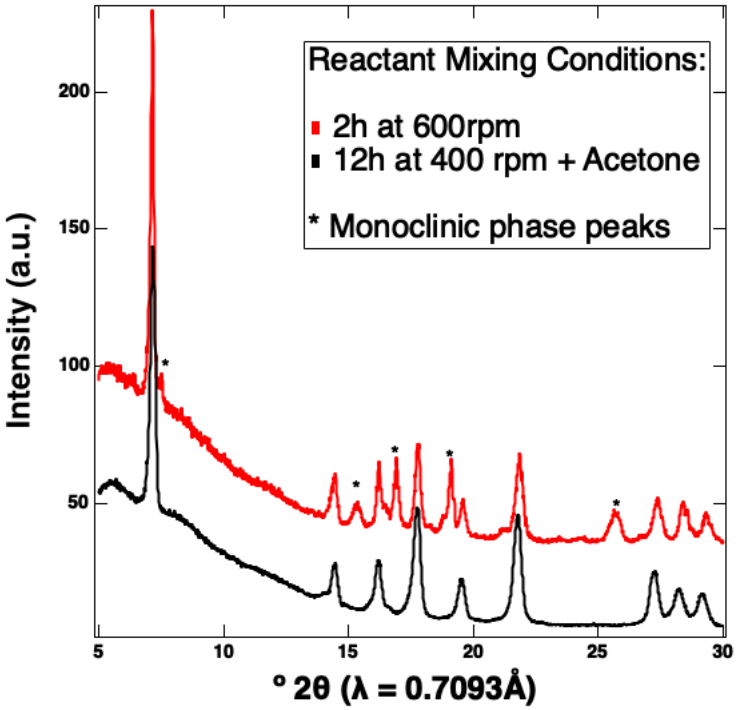

Figure 4. Powder XRD patterns measured for samples synthesized from precursor mixtures by two different mixing protocols. Asterisks indicate peaks of the secondary impurity phase.

When using this refined synthesis route, even a slight change in starting materials, such as using a new bottle of MnO_2, can lead to unwanted phase impurities. In this initial synthesis, stoichiometric ratios of $NaCH_3COO$ (99%) and previously used MnO_2 from Sigma-Aldrich (lot #1003401622) were combined, according to the outlined methods, and heated for 2 hours at 500°C, followed immediately by 10 hours at 900°C at a ramp rate of 5°C/min with a final cooling step to 250°C, at a controlled rate of 5°C/min. With only one variation, using a new bottle of MnO_2 (Sigma-Aldrich, Lot #1003805061) instead of the older one, we observed a monoclinic α-NMO phase impurity (*s.g. C2/m)* in the product, shown in Figure 5. Both MnO_2 compounds were purchased from Sigma-Aldrich and were found to be of the same orthorhombic phase (space group *Pnma*) with no impurities. Many synthesis alterations were done to reproduce the synthesis of phase pure P2 products using the new MnO_2, including a variation of secondary

heating temperatures (820°C – 940°C) in addition to the rate of cooling. XRD patterns collected for samples synthesized at different temperatures show a uniform monoclinic phase impurity, indicating the synthesis temperature within the range of 820°C – 940°C has little importance to the purity of the NMO when cooled at 5°C/min. A pure P2-NMO sample is included in Figure 5 as a reference.

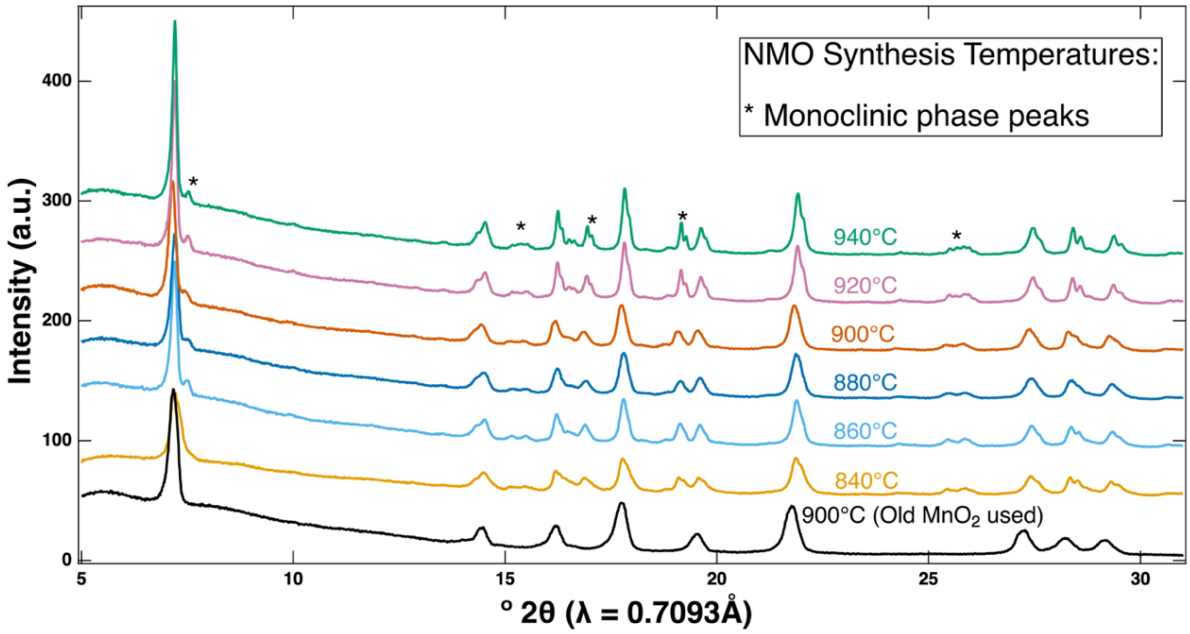

Figure 5. Powder XRD patterns measured for samples synthesized at different temperatures between 840-940°C. Asterisks indicate peaks of the secondary impurity phase.

Furthering the investigation to cooling rate modification, both decreasing and increasing the rate of cooling the sample from 900°C was tested. Significantly increasing the rate of cooling by quenching the NMO sample to room temperature from high temperatures of ≥ 900°C results in a pure orthorhombic phase (space group *Cmcm*), which corresponds to the high temperature (>1000°C) P'2 phase reported in the literature.[38,39] This result shows that the sample is phase pure before the cooling step; therefore, decreasing the rate of cooling was attempted to allow for the lower temperature thermodynamically stable phases to be observed. When decreasing the cooling rate from 5°C/min to 2.5°C/min, the P2 hexagonal structure was replicated with the new

bottle of MnO_2 precursor, shown in Figure 6. Therefore, the cooling rate has a significant impact on the phase purity of the NMO product. For a meta-stable phase like the P2 hexagonal NMO, a slower cooling rate is preferable.[39] Even with the new MnO_2, a phase-pure P2-NMO could be achieved. Figure 6 shows how slight changes in the synthesis methods (using new *versus* old MnO_2, and cooling rates of 2.5°C/min *versus* 5°C/min) can influence the phase purity of the product. This study has found the synthesis optimization of hexagonal P2 to be dependent on the homogeneity of the precursor compounds and the rate of cooling after the second heating step.

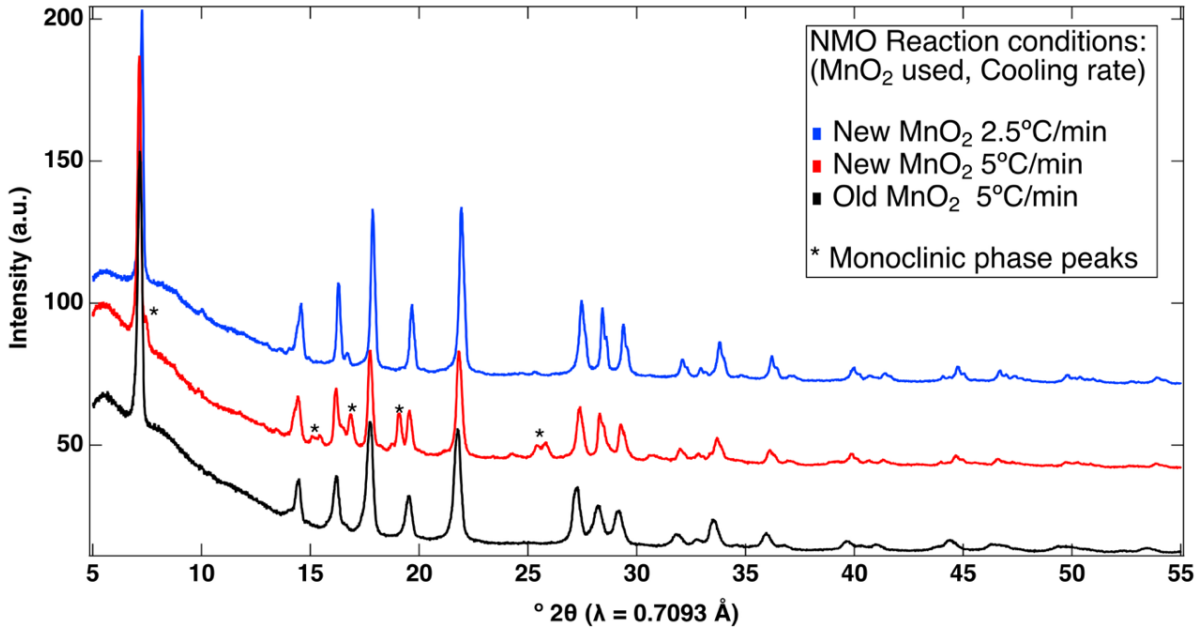

Figure 6. Powder XRD patterns for samples prepared from different precursor materials and synthesized at alternate cooling rates. Asterisks indicate peaks of the secondary impurity phase.

Ca-pillared NMO

For the incorporation of calcium into the structure of NMO, first, a direct synthesis method was tested by mixing stoichiometric amounts of $NaCH_3COO$, MnO_2, and CaO (Alfa Aesar) in a ball mill with acetone and performing the solid-state synthesis with the previously outlined methods.[30] Shown in Figure 7 is the XRD of a direct-synthesized Ca15%-NMO material. Multiple different phases, but not the desired hexagonal P2 structure, were seen in the product.

Phase identification refinement was not performed on the direct synthesis sample. It is hypothesized that a direct substitution synthesis of Ca for Na is not possible at the high temperatures required for the formation of the layered phase due to unfavorable thermodynamics.[31] Further investigation into the direct synthesis method was not performed.

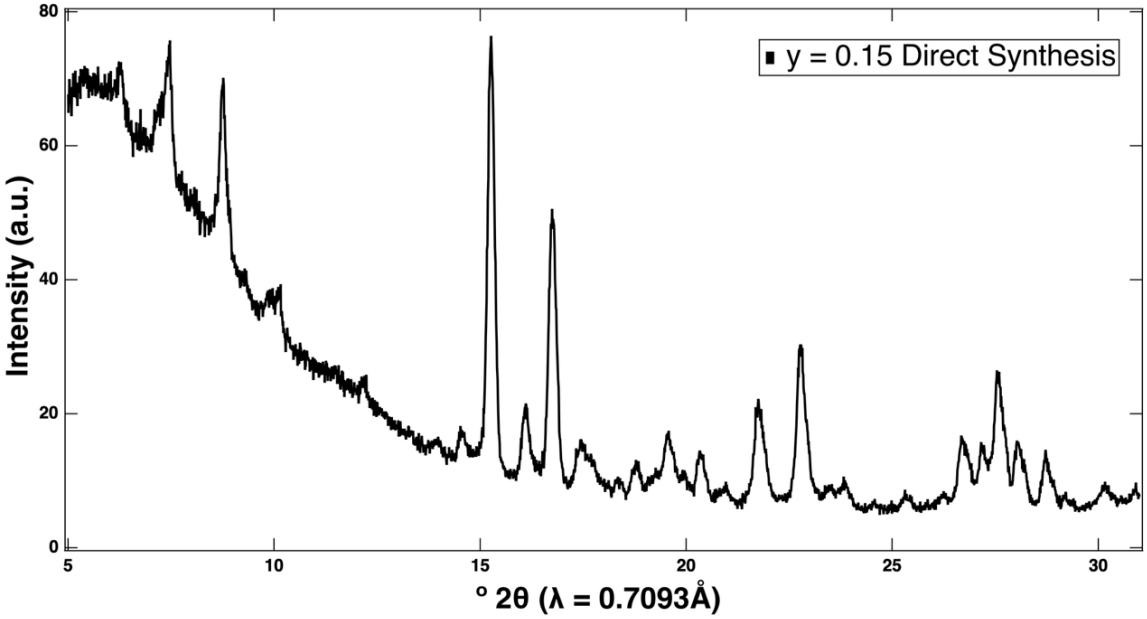

Figure 7. Powder XRD pattern of a y = 0.15 sample synthesized using a direct synthesis method.

Therefore, an ion exchange method was adopted from a previous work on Ca substitution in P2-$Na_xCa_yFe_{0.5}Mn_{0.5}O_2$.[31] This synthesis reported the mixing of his material with $Ca(NO_3)_2$ before pelletizing and heating in a tube furnace for 48 h at 300°C under flowing O_2 before repeated washing with ethanol.[31] For this study, stoichiometric amounts of as-synthesized NMO and anhydrous $Ca(NO_3)_2$ (10% excess) were mixed using a mortar and pestle in a glovebox. The mixed powders were then pelletized and heated to 300°C for 48h under flowing O_2. After cooling to room temperature, the samples were ground into a powder and washed in DI water. After washing and drying the cathode material, inductively coupled plasma optical emission spectrometry (ICP-OES) was carried out to analyze the specific stoichiometry of the synthesized

Ca5%-NMO sample. The total Mn content was used as a reference for ICP-OES analysis due to the probable absence of Mn impurities, leading to a consistent 1.0 molar ratio. Results for the measured elements are shown in Table 1. Limited by the functionality of the ICP-OES instrument on site, only the pristine NMO and Ca5%-NMO samples were analyzed for their stoichiometric composition.

Table 1. Elemental concentrations determined from ICP-OES.

Samples	Relative Element Fraction	
	Na/Mn	Ca/Mn
NMO	0.65	——
Ca5%-NMO	0.42	0.065

Equation 1 outlines the chemical reaction and evolution of the $NaNO_3$ byproduct during the Ca-ion exchange. In accordance with this equation, we should expect that an amount of 0.05 Ca should remove 0.10 Na, yet we observe a decrease of over 0.20 Na. This is hypothesized to be partly due to some excess sodium evaporation during the additional heating cycle. While ICP-OES analysis confirmed the presence of Ca in the NMO samples after ion exchange and wash, steps were taken to refine the ion-exchange methods. Factors such as the required atmosphere and the duration of synthesis affect the efficiency and cost-effectiveness of an experiment.[44] First, the exchange synthesis was repeated in air, without the flow of oxygen. As shown in Figure 8, the in-air synthesis, heated for 48 hours, produced almost identical XRD scans, which provided evidence of the CaX%-NMO materials' viability to be synthesized in air instead of oxygen. Furthermore, a synthesis conducted for 24 h was compared to that of a 48 h scan, where the total $NaNO_3$ evolution during the exchange gave evidence of a finished reaction after just 24 h (Figure 8). These tests lead to the conclusion that the ion-exchange could be completed in just 24 hours.

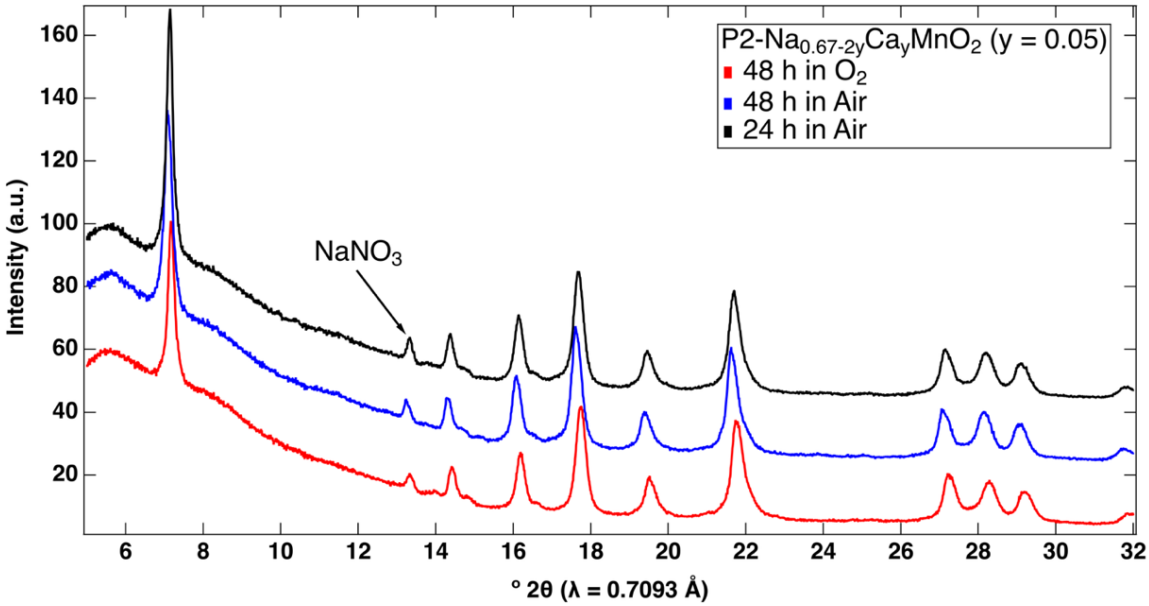

Figure 8. Powder XRD patterns for different synthesis atmospheres and lengths of the Ca-ion exchange, showing the evolution of equal amounts of the $NaNO_3$ salt formation.

With the need to wash the $NaNO_3$ salt out of the product after the exchange, different durations of a DI water rinse were tested. Initially, a 24 h wash was performed on the CaX%-NMO materials, but XRD characterization yielded evidence of the integration of H_2O into the structure, denoted as the "hydrated phase" shown in Figure 9. Subsequent durations of washing were tested and observed to completely remove the $NaNO_3$ from the product after only 10 minutes of washing, with no evidence of a hydrated phase. Figure 9 shows these washing durations in addition to the pre-washed sample that includes the $NaNO_3$ peak. These washing tests allowed for the Ca-ion exchange method to be further refined to a more efficient and quicker synthesis. To conclude, the Ca-ion exchange methods were refined to a heating scheme of 300°C for 24 h, followed by grinding and a 10-minute DI water wash.

$$Na_{2/3}MnO_2 + yCa(NO_3)_2 \rightarrow Na_{2/3-2y}Ca_yMnO_2 + 2yNaNO_3 \quad \textbf{Equation 1}$$

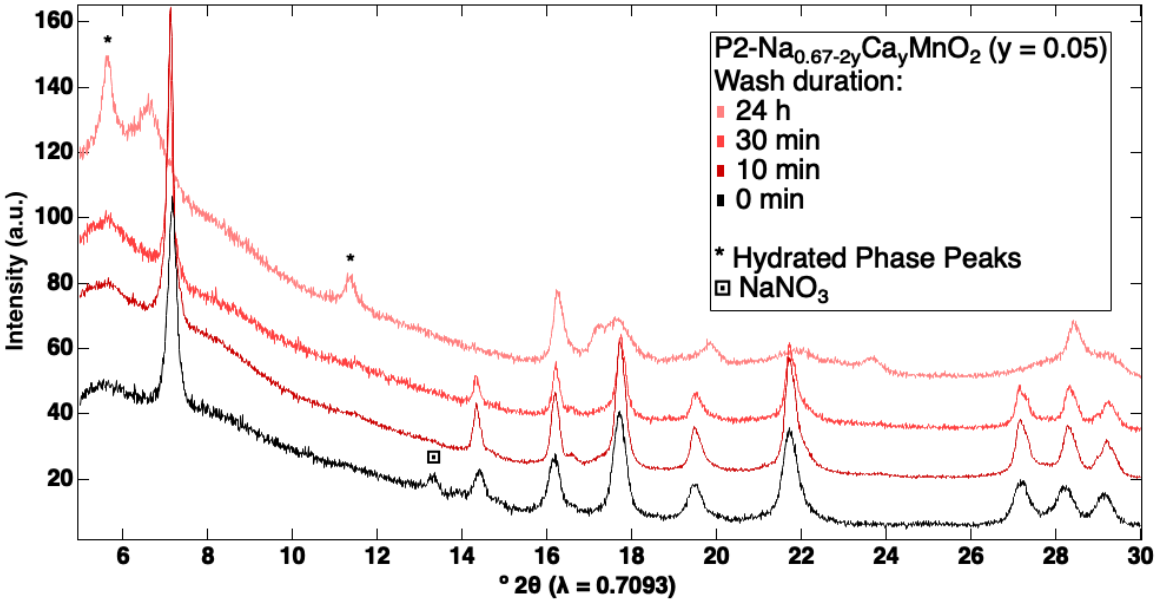

Figure 9. Different DI water wash durations for post-ion-exchange samples are shown with Powder XRD data of the Ca5%-NMO sample.

Phase Miscibility Gap in P2-$Na_{0.67-2y}Ca_yMnO_2$

Maintaining the P2 hexagonal structure of the NMO material post Ca-ion exchange is important for evaluating the electrochemical performance of the substituted cathode. In-house lab XRD showed peak broadening with increased calcium concentrations, which was hypothesized to be a phase separation between Na-rich and Ca-rich domains. Figure 10 shows the lab XRD patterns of NMO and the substituted samples with apparent peak broadening.

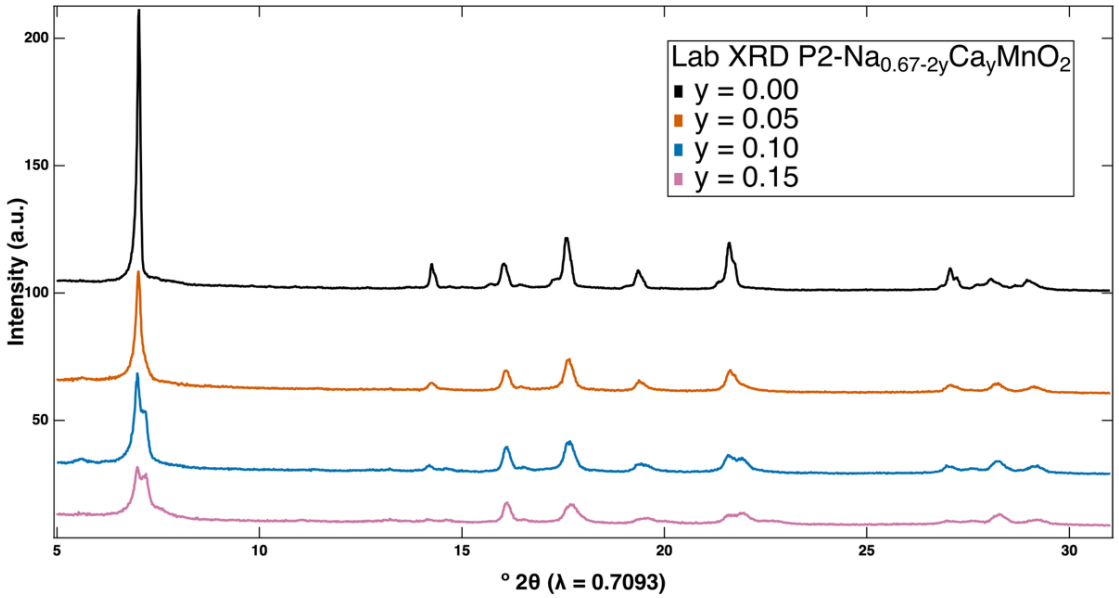

Figure 10. Powder XRD patterns of y = 0.00-0.15 samples taken in the lab with a Mo Kα source.

To obtain better resolution of a possible phase separation, synthesized materials of pristine NMO and CaX%-NMO (X = 5, 10, and 15) were sent to the synchrotron for beamline XRD analysis at Brookhaven National Laboratory. Further synchrotron characterization allowed for the refinement of two separate P2 phases present in the substituted samples. Figure 11 shows the XRD patterns for a range of P2-$Na_{0.67-2y}Ca_yMnO_2$ samples, with y = 0, 0.05, and 0.10. When observing the (002), (004), and (100) peaks of the hexagonal P2 crystal system (Figure 11d), the second P2 phase is shown to be more intense with higher Ca-substituted materials. One possible explanation for the apparent phase separation is a change in the interlayer spacing. Previous studies involving the substitution of Ca into the prismatic sodium sites have shown that low doping levels of Ca can lead to a decrease in the *c*-lattice parameter.[45] Although Ca^{2+} replaces two Na^+ ions during the ion exchange, its greater localized coulombic charge may be responsible for the reduction in interlayer spacing.[46] The uneven distribution of Ca ions throughout the substituted samples is thought to be partly responsible for the peak separation observed. A miscibility gap refers to the region on a phase diagram where two or more phases do not

completely mix, resulting in a two-phase system that can be observed through XRD characterization techniques.[47,48] In the case of this study, the two phases present are proposed to be a Na-rich phase and a Ca-rich phase, caused by the uneven distribution of Ca ions during the ion-exchange.

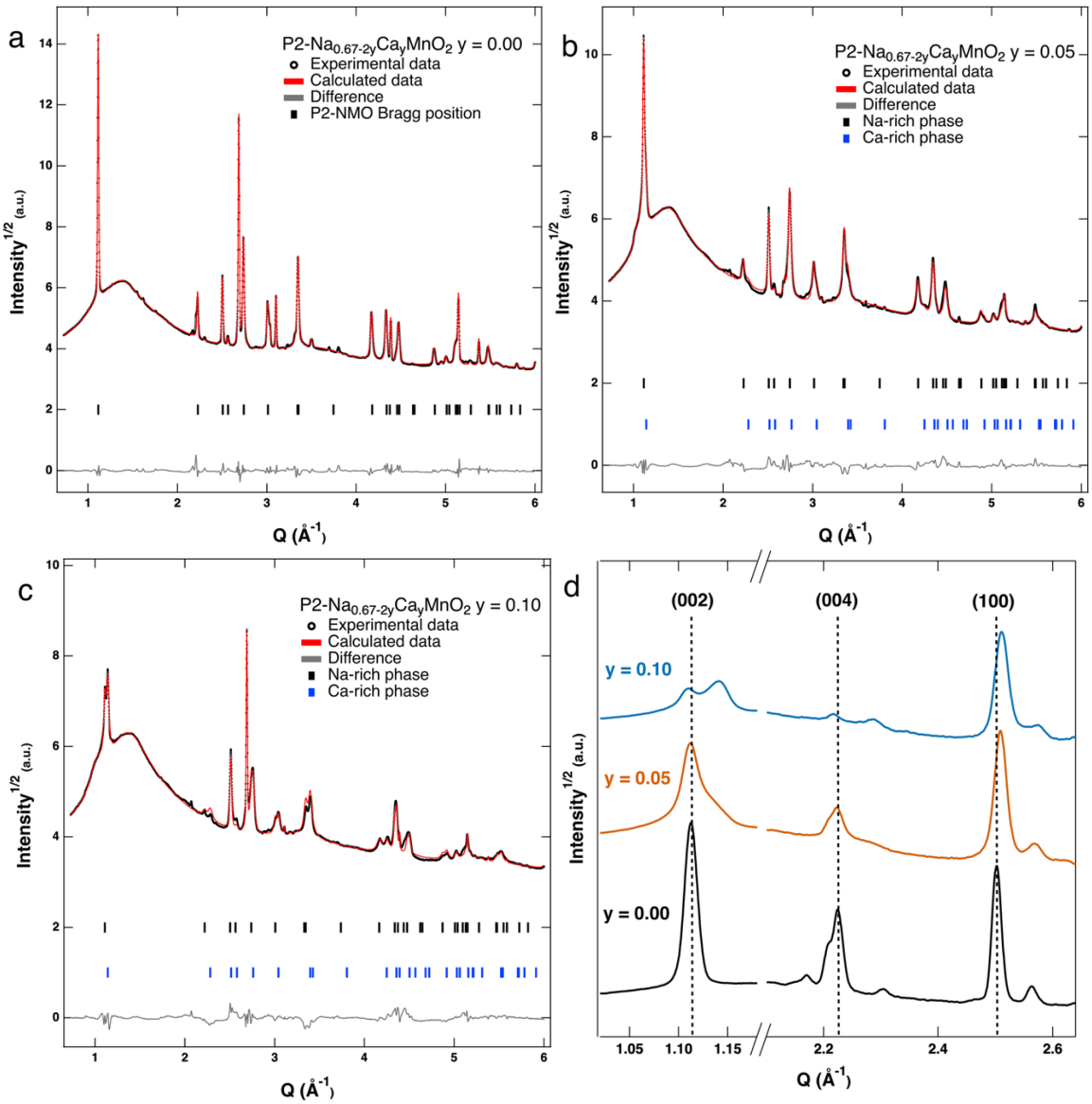

Figure 11. Rietveld refinement results of synchrotron XRD data for (a) y = 0.00, (b) y = 0.05, and (c) y = 0.10 in P2-$Na_{0.67-2y}Ca_yMnO_2$. (d) Comparison of (002), (004), and (100) peaks from the for y = 0.00, 0.05, and 0.10 materials.

To evaluate this hypothesis, an additional annealing step was performed on the substituted samples. Annealing to a higher temperature than the ion-exchange was initially performed can

allow for a more uniform phase to be thermodynamically favorable. After heating to a higher temperature of 500°C for 2 h, the samples were quenched to room temperature. This quenching step is important because it locks in the higher temperature phase, assuming that the diffusion kinetics are low for Ca at room temperature. Powder XRD measurements for y = 0.05 AQ and y = 0.10 AQ samples were performed with a Cu x-ray source (λ = 1.5418 Å) with the intention of observing further d-space separation due to a longer wavelength. Figure 12 shows the (002) peak of the y = 0.05 and 0.10 samples before and after re-annealing. Further investigation of the Ca15%-NMO was of little interest due to the phase impurities brought on by annealing.

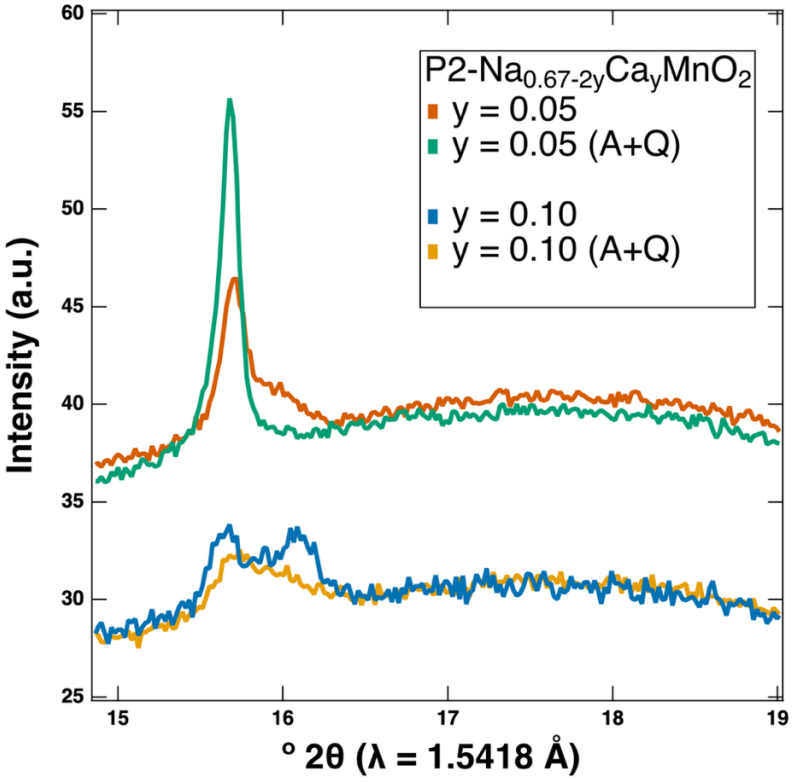

Figure 12. Powder XRD data for the Ca5%-NMO sample in the range of 15 - 17°, before and after the anneal-quench step. Collected using Cu K α radiation.

Electrochemistry

Galvanostatic charge/discharge cycles were performed on the cathode materials. Voltage profiles for the non-annealed samples (y = 0.00, 0.05, 0.10, 0.15) during the 2nd charge/discharge are

shown in Figure 13. Changes in the slope of these voltage profiles can be an indication of structural changes occurring within the cathode material. Looking at the NMO material (y = 0.00) in Figure 13, there is a moderate voltage plateau around 4.0-4.4V during the charging cycle, which can be an indication of a phase change. Additionally, when comparing the y = 0.00 material to the substituted samples, we can see that this upper voltage plateau gets smoother, which can be evidence of the reduction of this specific phase change region. It should be noted that within the 2.1-2.3V window, there are sharp dips in the voltage profile of some of the substituted materials, which could be a result of trace water impurities.

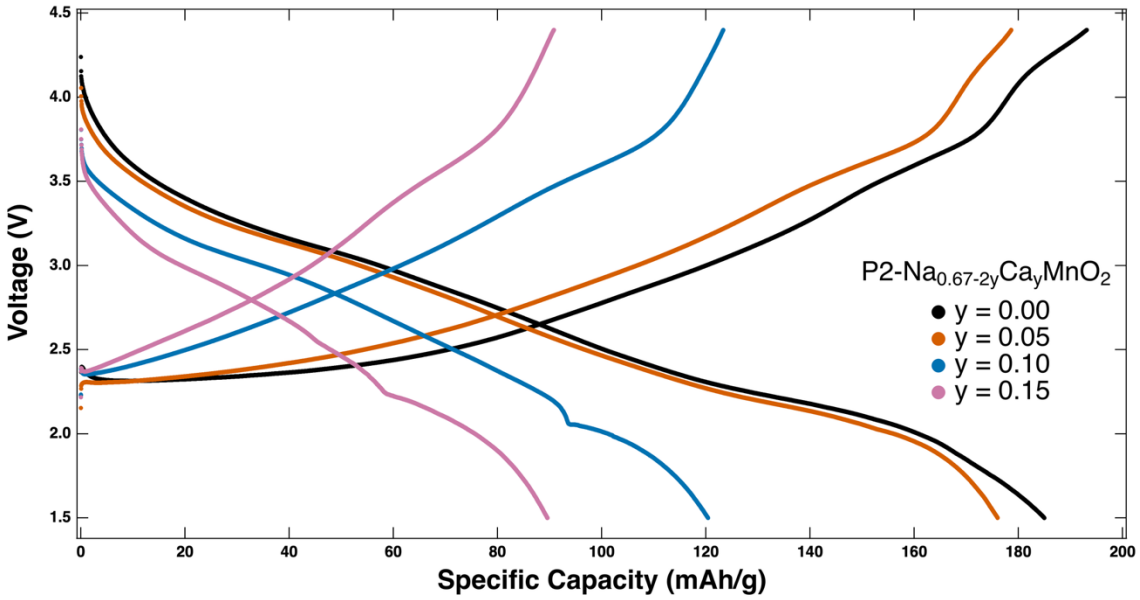

Figure 13. Voltage profiles for $Na_{0.67-2y}Ca_yMnO_2$ materials at C/20 for 243 mAh/g during the second charge/discharge cycle.

The long-term cycling performance of the P2-$Na_{0.67-2y}Ca_yMnO_2$ materials was measured for samples without the additional anneal-quench step (Figure 14). These tests were evaluated in the voltage range of 1.5-4.4V at a rate of C/20. The initial specific capacity of the pristine NMO, y = 0.00, was 193 mAh/g, which outperformed the Ca-substituted samples. However, the y = 0.00 sample experiences significant capacity degradation within the first 5 cycles and follows the

degradation characteristics of the y = 0.05 material. It can be observed that the y = 0.05 sample outperforms the pristine NMO after just 30 cycles and continues to proceed with steady degradation through 125 cycles. Past the 30-cycle benchmark, the NMO material loses capacity at a faster rate than any of the Ca-substituted materials. Additionally, with more Ca substitution, the overall specific capacity of the material decreases. This is due to Ca^{2+} ions occupying the space of two Na^{+} ions. While these calcium ions stay behind in the cathode and allow for a more rigid structure, the theoretical capacity of the material is reduced due to the ions not participating in the charge migration.[49] The comparison between the substituted and unsubstituted samples shown in Figure 10 yields evidence of a positive relationship between capacity retention and Ca-substitution for ≥ 40 cycles with respect to the y = 0.00 and 0.05 samples. These findings align with previous studies on Ca-doped Na_xCoO_2 conducted by Han *et al.,* which also demonstrate improvement in cycling stability in Ca-doped sodium-based materials.[32]

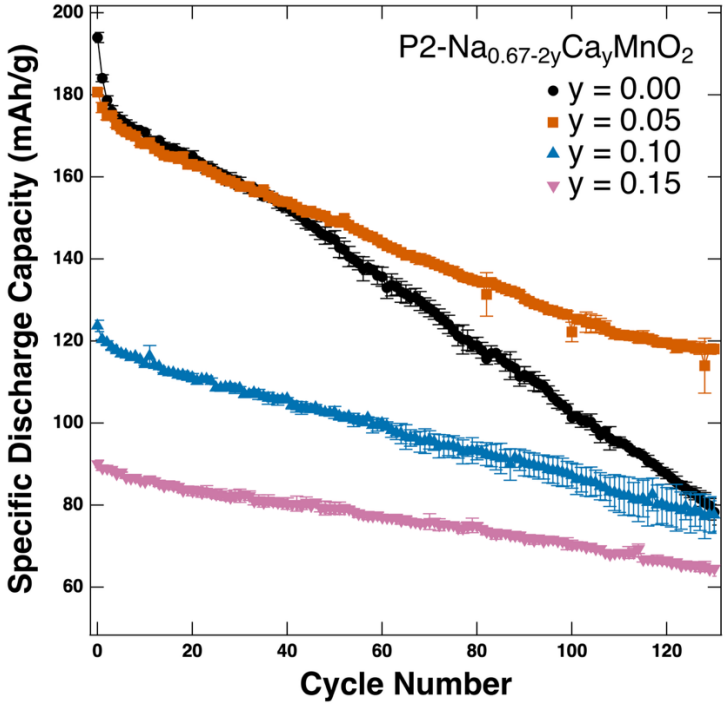

Figure 14. Average cycle performance of P2-$Na_{0.67-2y}Ca_yMnO_2$ materials at C/20 for a theoretical capacity of 243 mAh/g. Error bars include the standard deviation of 2-3 cells.

Additional long-term cycling of the annealed-quenched (AQ) samples was tested under the same electrochemical parameters. The voltage profiles of the AQ samples appear very similar to the non-annealed samples (Figure 15).

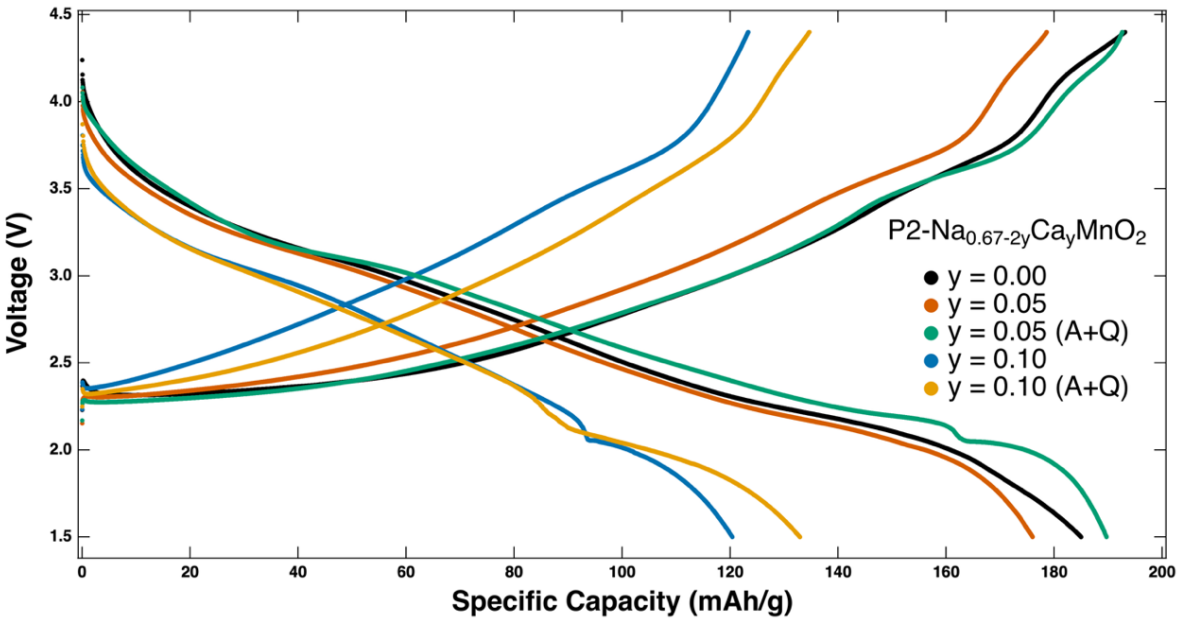

Figure 15. Voltage profiles for y = 0.00, y = 0.05, and y = 0.10 $Na_{0.67-2y}Ca_yMnO_2$ materials, including AQ samples, at C/20 for 243 mAh/g during the second charge/discharge cycle.

Figure 16a shows the additional benefits of the secondary AQ step for the y = 0.05 and 0.10 samples, as it appears to increase the overall specific discharge capacity while still maintaining a slower degradation rate than the pristine NMO material. The y = 0.10AQ sample observed a specific discharge capacity of 118 mAh/g and a capacity retention of 87% after 100 cycles in comparison to the non-annealed sample, 89.8 mAh/g with 72% retention after 100 cycles. When looking at the y = 0.05 samples, the capacity retention after 100 cycles is the same, 70%, yet the capacity of the AQ sample is about 10-15 mAh/g higher than the non-annealed material. These differences in capacity can be due to slight variations within the AQ samples, such as a reduced water impurity in the cells. Figure 16b shows the specific energy density (Wh/kg) of the samples.

It's observed to be a linear decrease in energy density for the Ca-substituted samples over 100 cycles, with a stronger decrease in the as-synthesized NMO after just 40 cycles.

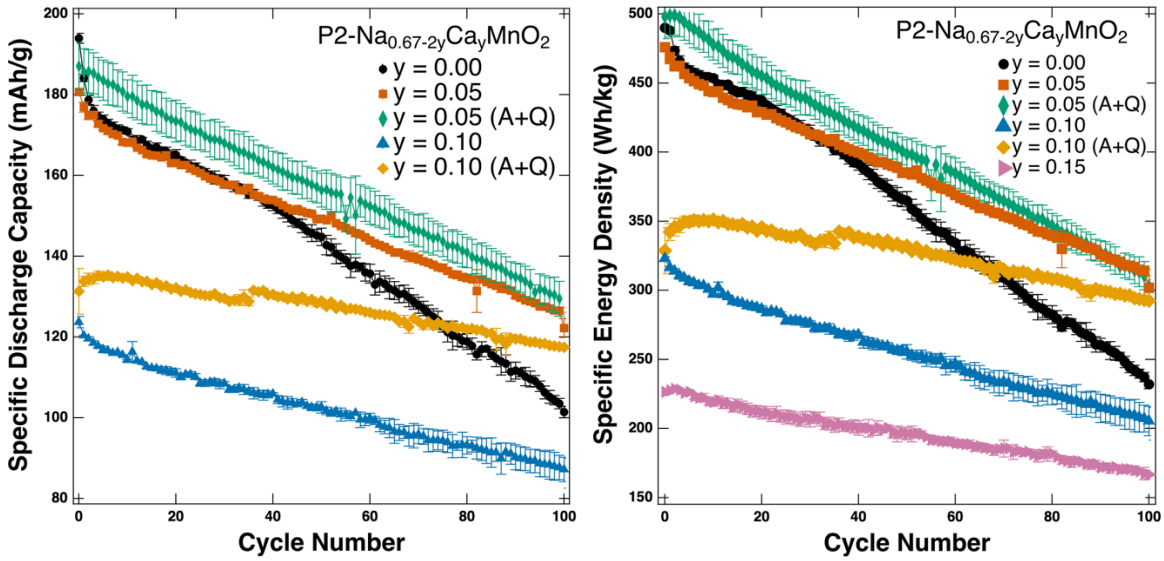

Figure 16. (a) Average cycle performance of AQ P2-$Na_{0.67-2y}Ca_yMnO_2$ materials compared with as-synthesized Ca-substituted materials. (b) Average specific energy density for all P2-$Na_{0.67-2y}Ca_yMnO_2$ materials. All cells cycled at C/20 for a theoretical capacity of 243 mAh/g, with error bars showing the standard deviation across 2-3 similar cells.

A rate test was performed on the pristine NMO and the highest performing Ca-substituted material (y = 0.05AQ). Charging and discharging cycles from 0.1C to 5C were conducted in groups of five cycles before increasing the rate. After completing the 5C cycles, the cells reverted to cycling at 0.1C for five more cycles. It can be seen in Figure 17 that at all rates of charging and discharging, the y = 0.05AQ sample performed higher and with more stability than the unsubstituted material.

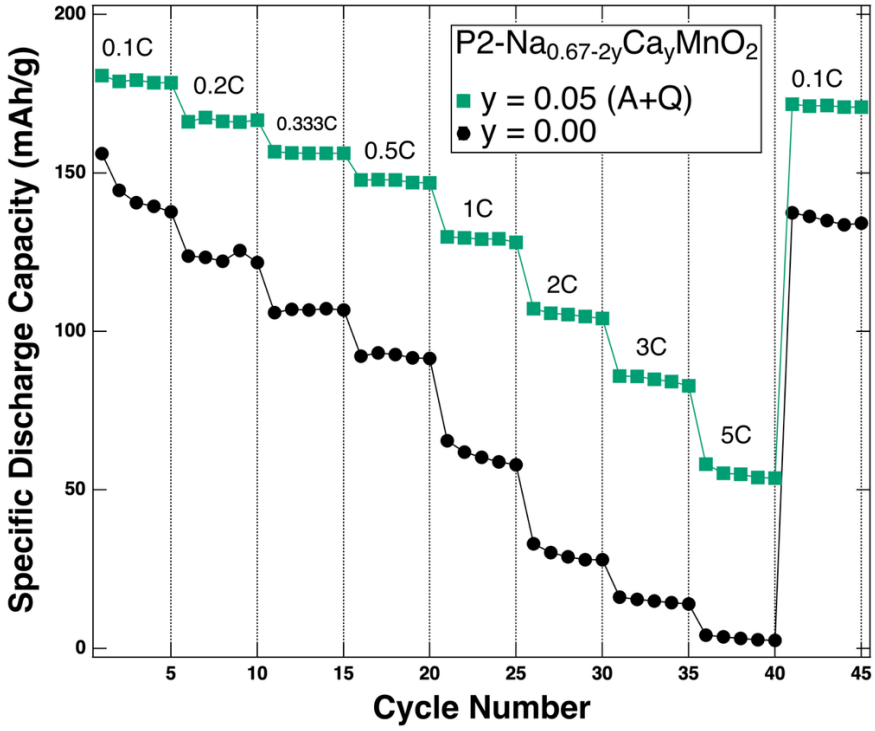

Figure 17. Rate performance of y = 0.00 and y = 0.05 (A+Q) materials.

Phase transition during electrochemical cycling

In-operando XRD is a valuable technique for characterizing battery materials that allows for tracking the structural development of the cathode during charging and discharging cycles. Operando experiments enable analysis of mechanisms, phase transitions, and insights into capacity fade and mechanical failure.[50–53] This study uses in-operando XRD characterization, conducted at the synchrotron at Brookhaven National Laboratory by Anthony T. Pacileo, on the y = 0.00 and 0.05 materials before annealing. The operando cells were cycled at C/10 with an average mass loading of 21 mg/cm². Custom coin cells were made with slits in the casing to allow the X-ray beam to pass through the cell. A higher mass loading is preferred to increase scattering and overall intensity. The second cycle of each cell is shown in Figure 18 below within the 2θ range of 1.6–2.2°2θ (λ = 0.1811). Single peak refinement was used in an attempt to analyze the lattice parameters of the phases present during cycling. The pristine NMO material,

Figure 18a, shows multiple phase changes at both low and high voltages. When charged to 4.3V, the extraction of Na^+ ions promotes the gliding of MnO_6 layers, causing a phase change from P2 to OP4.[30] When Na^+ ions are re-intercalated, a phase change from P2 to P'2 is observed at a lower voltage. These phase change locations are labeled within Figure 18a. Previous studies confirm the same phase transitions in NMO through similar in-operando XRD techniques.[30] Observations of lattice parameters for the y = 0.00 material are shown in Figure 19a.

While single peak fitting was also used on the y = 0.05 sample, it is more difficult to identify and analyze the different phases present. Figure 20 shows the structural evolution of peaks within the 2θ range of 1.6–2.2 °2θ (λ = 0.1811) and illustrates the limited separation of these peaks when charged to 4.3 V. Additionally, Figure 21 shows the XRD patterns of the y = 0.00 and 0.05 samples in the charged state at 4.3V. The resolution between the peaks for the 0.00 material is significantly better than that of the 0.05 material. Synchrotron XRD data revealed that this sample was composed of two separate P2 phases, which are hypothesized to be Na-rich and Ca-rich P2 phases. This further complicates the specific refinement since we are unable to distinguish the phases from each other during cycling. Single peak refinement can allow us to obtain structural lattice parameters from the hypothesized (002) peaks within this region, but we are unable to determine the identity of these phases. At the high voltages, the substituted sample is observed to have three peaks corresponding to the P2, Z, and OP4 phases. The TM-TM interlayer distance can be seen for these phases in Figure 19b. The low voltage yields an additional small peak, which was refined and labeled as the U phase. Evidence of pillaring can be seen by the reduction of phase separation at the high and low voltages shown by operando XRD. However, we are unable to obtain a complete understanding of the pillaring effect due to

the presence of multiple P2 phases in the y = 0.05 starting material.

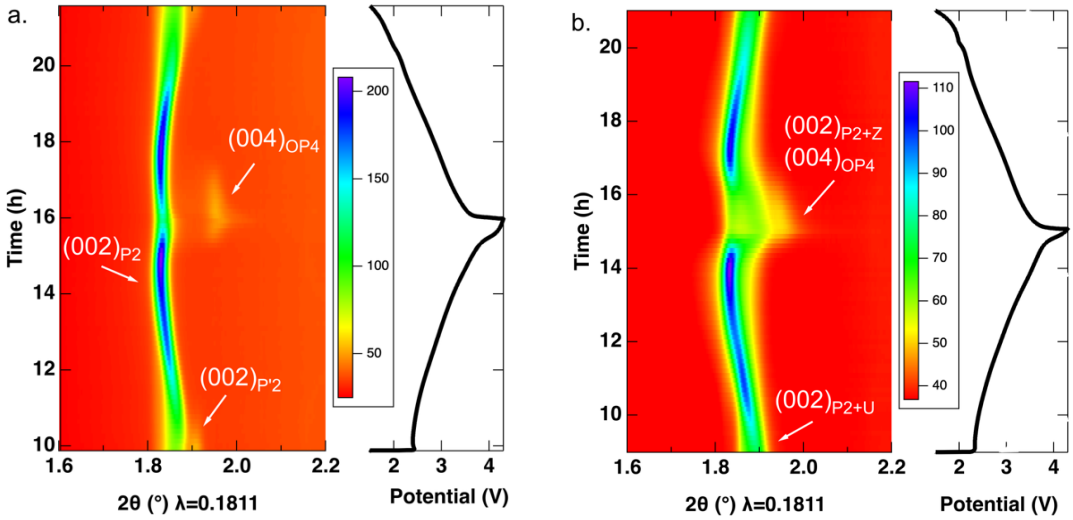

Figure 18. Operando XRD measurement of the (002) peak reflection for (a) y = 0.00 and (b) y = 0.05 cathode materials during the second full cycle in the voltage window of 1.5V to 4.3V.

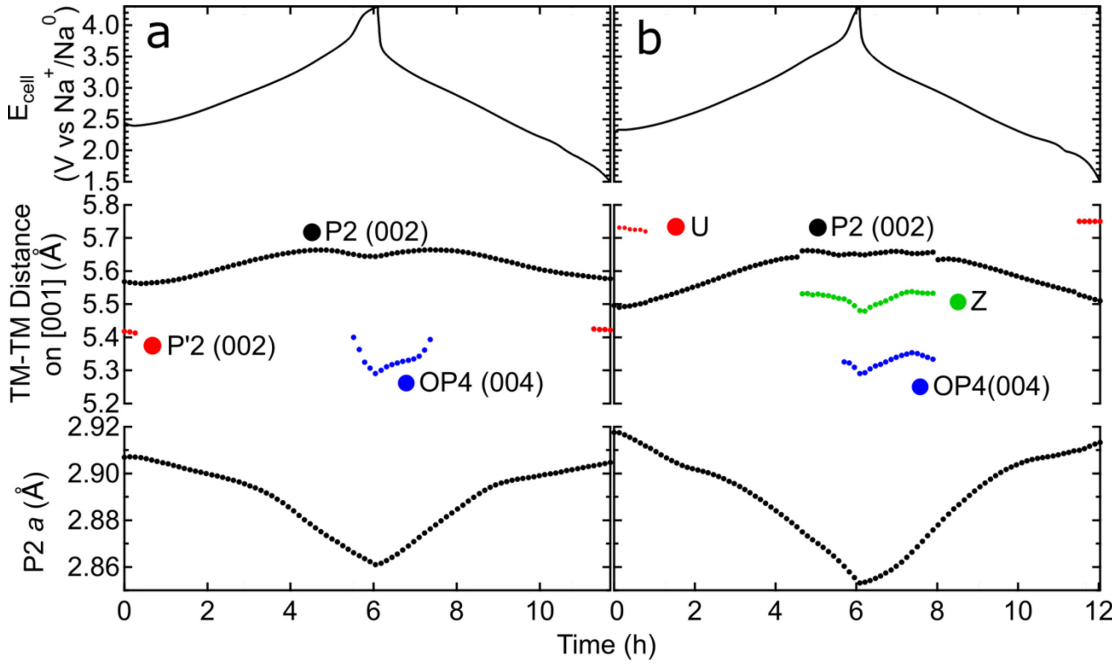

Figure 19. Refined unit cell parameters for the phases in the (a) y = 0.00 and (b) y = 0.05 materials during the second full cycle in the voltage window of 1.5V to 4.3V.

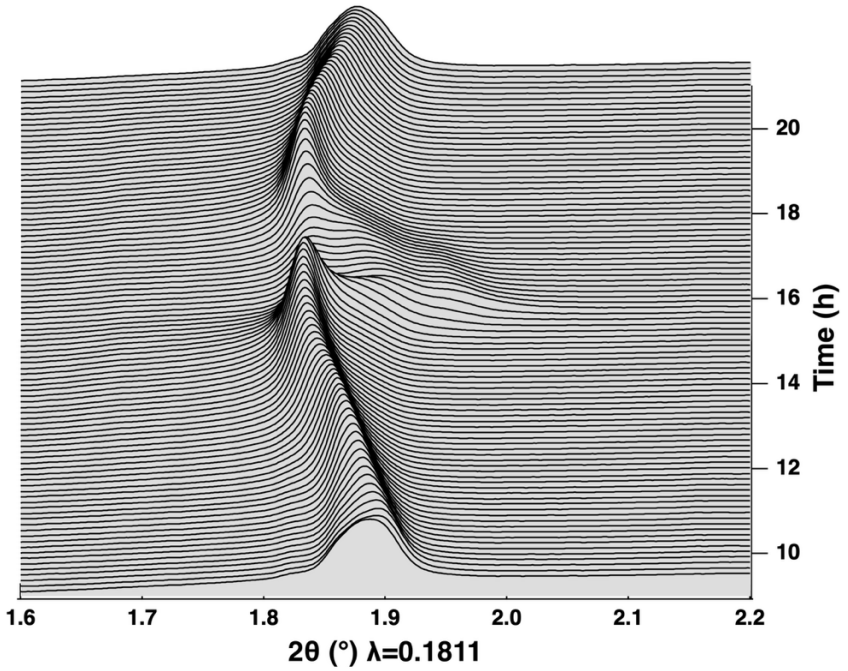

Figure 20. Operando XRD patterns corresponding to the second charge and discharge cycle for the y = 0.05 sample within the 2θ range of 1.6–2.2°2θ (λ = 0.1811).

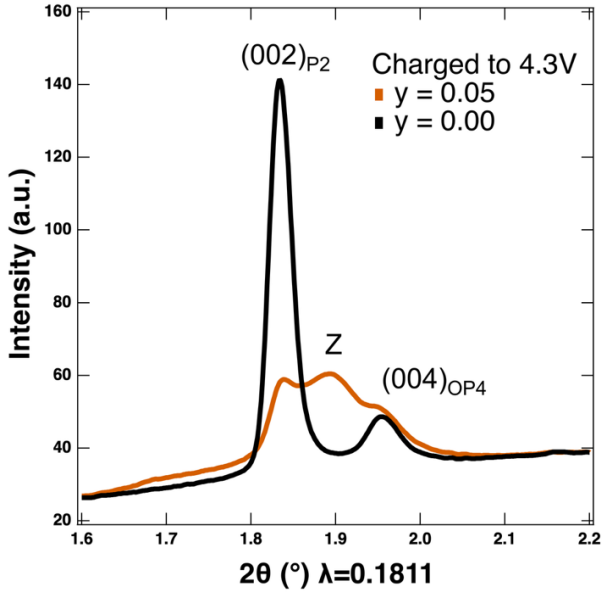

Figure 21. XRD pattern of the y = 0.00 and 0.05 material in the charged state at 4.3V within the 2θ range of 1.6–2.2°2θ (λ = 0.1811).

Conclusions

The results of this study report a tunable solid-state synthesis for the phase-pure P2-NMO cathode material. Additionally, a refined method for the partial substitution of calcium into the layered structure was recorded. This investigation observed that with higher levels of Ca substitution, there was a phase splitting into two separate P2 phases.

This study has identified one possible explanation for the phase splitting observed when increasing the substitution level of Ca. It is hypothesized that the Ca-ions do not completely diffuse during the exchange and therefore create areas of a Ca-rich lattice and Na-rich structure. This is one possible explanation for the observed lattice decrease seen when increasing the amount of calcium substitution. An additional anneal-quench step has been reported in this study to decrease the phase miscibility gap between the two P2 phases observed through powder XRD. Long-term cycling of the P2-$Na_{0.67-2y}Ca_yMnO_2$ materials shows a decrease in starting capacity due to the Ca ions that occupy the redox inactive sites of Na^+ after substitution. Cycling shows the y = 0.05 and 0.05(A+Q) samples outperform the as-synthesized NMO, showing a positive pillaring effect at this doping level.

Operando XRD studies yielded consistent results with previous literature for the NMO sample.[30] However, the y = 0.05 sample was not a single-phase cathode material and therefore was more difficult to analyze the phase evolution during cycling. Nonetheless, the y = 0.05 sample observes an overall decrease in lattice shift, which may be evidence of its pillared structure.

Future Work

This study does not address manganese dissolution, which is a common problem for SIBs. Further investigation into the manganese dissolution mechanism for the NMO material needs to be addressed, along with the influence that Ca-pillaring may have on this issue. Previous studies have had success using ZrO_2 as a coating on manganese-oxide cathodes to prevent such transition metal dissolution.[54]

A neutron diffraction proposal has been submitted for the unsubstituted and AQ samples. Neutron diffraction patterns allow for specific site occupancies to be observed and will enable us to determine where the Ca ions are in the material. This insight into the distribution of Ca within the material can provide information on the effectiveness of the anneal-quench step at diffusing the Ca into the layered structure.

In-operando XRD studies of the AQ samples will be a more informative method for observing the phase changes present during the cycling of the substituted materials. It can show the difference between the two-phase and a single-phase substituted material and can shed light on the reaction mechanism for a pillared cathode.

Additionally, ICP-OES analysis is necessary for the Ca-substituted materials and was not performed in this study due to some functionality issues with the instrument. This analysis can provide further insight into the substitution limitations. Although the Ca-ion substitution reaction was successful, further optimization may be performed to eliminate the anneal-quench step reported in this study. Increasing the ion-exchange reaction temperature to 500°C may allow for

the complete diffusion of Ca into the P2-NMO in favor of the formation of a single phase. However, the decomposition temperature of the evolved $NaNO_3$ salt is 380°C, which may introduce impurities in the sample. Additionally, the investigation of the Ca solubility in NMO can be determined by increasing the dopant levels until the layered structure can no longer substitute for Ca. Furthermore, Ca-doping has been known to improve the water and air stability of different LTMOs.[31,55] Subsequent stability experiments can be performed on the P2-$Na_{0.67-2y}Ca_yMnO_2$ materials to identify any atmospheric stability improvement.

References

(1) Yabuuchi, N.; Kubota, K.; Dahbi, M.; Komaba, S. Research Development on Sodium-Ion Batteries. *Chem. Rev.* **2014**, *114* (23), 11636–11682. https://doi.org/10.1021/cr500192f.

(2) Kulka, A.; Marino, C.; Walczak, K.; Borca, C.; Bolli, C.; Novák, P.; Villevieille, C. Influence of Na/Mn Arrangements and P2/P′2 Phase Ratio on the Electrochemical Performance of NaxMnO2 Cathodes for Sodium-Ion Batteries. *J. Mater. Chem. A* **2020**, *8* (12), 6022–6033. https://doi.org/10.1039/C9TA12176E.

(3) Whittingham, M. S. Lithium Batteries and Cathode Materials. *Chem. Rev.* **2004**, *104* (10), 4271–4302. https://doi.org/10.1021/cr020731c.

(4) Whittingham, M. S. Electrical Energy Storage and Intercalation Chemistry. *Science* **1976**, *192* (4244), 1126–1127. https://doi.org/10.1126/science.192.4244.1126.

(5) Monroe, D. Building a Better Battery. *MRS Bulletin* **2020**, *45* (3), 246–247. https://doi.org/10.1557/mrs.2020.81.

(6) Brandt, K. Historical Development of Secondary Lithium Batteries. *Solid State Ionics* **1994**, *69* (3–4), 173–183. https://doi.org/10.1016/0167-2738(94)90408-1.

(7) Koch, V. R. Status of the Secondary Lithium Electrode. *Journal of Power Sources* **1981**, *6* (4), 357–370. https://doi.org/10.1016/0378-7753(81)80040-7.

(8) Mizushima, K.; Jones, P. C.; Wiseman, P. J.; Goodenough, J. B. LixCoO2 (0<x<-1): A New Cathode Material for Batteries of High Energy Density. *Materials Research Bulletin* **1980**, *15* (6), 783–789. https://doi.org/10.1016/0025-5408(80)90012-4.

(9) Yoshino, A. The Lithium-Ion Battery: Two Breakthroughs in Development and Two Reasons for the Nobel Prize. *bull. Chem. Soc. Jpn.* **2022**, *95* (1), 195–197. https://doi.org/10.1246/bcsj.20210338.

(10) Yoshino, A. From Polyacetylene to Carbonaceous Anodes. *Nat Energy* **2021**, *6* (4), 449–449. https://doi.org/10.1038/s41560-021-00801-0.

(11) Nishi, Y. The Dawn of Lithium-Ion Batteries. *Interface magazine* **2016**, *25* (3), 71–74. https://doi.org/10.1149/2.F06163if.

(12) Kaunda, R. B. Potential Environmental Impacts of Lithium Mining. *Journal of Energy & Natural Resources Law* **2020**, *38* (3), 237–244. https://doi.org/10.1080/02646811.2020.1754596.

(13) Vera, M. L.; Torres, W. R.; Galli, C. I.; Chagnes, A.; Flexer, V. Environmental Impact of Direct Lithium Extraction from Brines. *Nat Rev Earth Environ* **2023**, *4* (3), 149–165.

https://doi.org/10.1038/s43017-022-00387-5.

(14) Zheng, L.; Chen, G.; Liu, L.; Hu, Y. Tracing of Lithium Supply and Demand Bottleneck in China's New Energy Vehicle Industry—Based on the Chart of Lithium Flow. *Front. Energy Res.* **2022**, *10*. https://doi.org/10.3389/fenrg.2022.992617.

(15) Halkes, R. T.; Hughes, A.; Wall, F.; Petavratzi, E.; Pell, R.; Lindsay, J. J. Life Cycle Assessment and Water Use Impacts of Lithium Production from Salar Deposits: Challenges and Opportunities. *Resources, Conservation and Recycling* **2024**, *207*, 107554. https://doi.org/10.1016/j.resconrec.2024.107554.

(16) Wang, H.; Yu, D.; Kuang, C.; Cheng, L.; Li, W.; Feng, X.; Zhang, Z.; Zhang, X.; Zhang, Y. Alkali Metal Anodes for Rechargeable Batteries. *Chem* **2019**, *5* (2), 313–338. https://doi.org/10.1016/j.chempr.2018.11.005.

(17) oc_admin. *Sodium-ion Batteries on the Horizon: Where Do They Challenge Lithium-ion?*. OneCharge. https://www.onecharge.biz/blog/sodium-ion-vs-lithium-ion-batteries/ (accessed 2025-02-18).

(18) Hwang, J.-Y.; Myung, S.-T.; Sun, Y.-K. Sodium-Ion Batteries: Present and Future. *Chemical Society Reviews* **2017**, *46* (12), 3529–3614. https://doi.org/10.1039/C6CS00776G.

(19) Mousavinezhad, S.; Sharifian, S.; Nikfar, S.; Vahidi, E. The Next Lithium Boom? Assessment of U.S. Domestic Production Pathways through Economic and Environmental Lenses. *Environ. Sci. Technol.* **2025**. https://doi.org/10.1021/acs.est.5c09948.

(20) Zhao, L.; Zhang, T.; Li, W.; Li, T.; Zhang, L.; Zhang, X.; Wang, Z. Engineering of Sodium-Ion Batteries: Opportunities and Challenges. *Engineering* **2023**, *24*, 172–183. https://doi.org/10.1016/j.eng.2021.08.032.

(21) Liu, J.; Zhang, N.; Shi, H.; He, Z.; Zhang, Z.; Anishchenko, D. V.; Alekseeva, E. V.; Li, R.; Yang, P.; Levin, O. V.; Wang, D.; Liu, H.; Dou, S.; Wang, B. Layered Transition Metal Oxide Cathodes for Sodium-Ion Batteries: Challenges, Progress, and Perspectives. *Chemical Engineering Journal* **2025**, *521*, 167111. https://doi.org/10.1016/j.cej.2025.167111.

(22) Wang, Y.; Wang, Y.; Xing, Y.; Jiang, C.; Pang, Y.; Liu, H.; Wu, F.; Gao, H. Entropy Modulation Strategy of P2-Type Layered Transition Metal Oxide Cathodes for Sodium-Ion Batteries with a High Performance. *J. Mater. Chem. A* **2023**, *11* (37), 19955–19964. https://doi.org/10.1039/D3TA04094A.

(23) Luong, H. D.; Dinh, V. A.; Momida, H.; Oguchi, T. Insight into the Diffusion Mechanism of Sodium Ion–Polaron Complexes in Orthorhombic P2 Layered Cathode Oxide NaxMnO2. *Phys. Chem. Chem. Phys.* **2020**, *22* (32), 18219–18228. https://doi.org/10.1039/D0CP03208E.

(24) Lu, J.; Zhang, J.; Huang, Y.; Zhang, Y.; Yin, Y.; Bao, S. Advances on Layered Transition-Metal Oxides for Sodium-Ion Batteries: A Mini Review. *Front. Energy Res.* **2023**, *11*. https://doi.org/10.3389/fenrg.2023.1246327.

(25) Zhao, Y.; Liu, Q.; Zhao, X.; Mu, D.; Tan, G.; Li, L.; Chen, R.; Wu, F. Structure Evolution of Layered Transition Metal Oxide Cathode Materials for Na-Ion Batteries: Issues, Mechanism and Strategies. *Materials Today* **2023**, *62*, 271–295. https://doi.org/10.1016/j.mattod.2022.11.024.

(26) Brennhagen, A.; Cavallo, C.; Wragg, D. S.; Sottmann, J.; Koposov, A. Y.; Fjellvåg, H. Understanding the (De)Sodiation Mechanisms in Na-Based Batteries through Operando X-Ray Methods. *Batteries & Supercaps* **2021**, *4* (7), 1039–1063. https://doi.org/10.1002/batt.202000294.

(27) Velikokhatnyi, O. I.; Chang, C.-C.; Kumta, P. N. Phase Stability and Electronic Structure of NaMnO2. *J. Electrochem. Soc.* **2003**, *150* (9), A1262. https://doi.org/10.1149/1.1600464.

(28) Wang, Y.; Feng, Z.; Cui, P.; Zhu, W.; Gong, Y.; Girard, M.-A.; Lajoie, G.; Trottier, J.; Zhang, Q.; Gu, L.; Wang, Y.; Zuo, W.; Yang, Y.; Goodenough, J. B.; Zaghib, K. Pillar-Beam Structures Prevent Layered Cathode Materials from Destructive Phase Transitions. *Nat Commun* **2021**, *12* (1), 13. https://doi.org/10.1038/s41467-020-20169-1.

(29) Kim, M. A.; Zimmerer, E. K.; Piontkowski, Z. T.; Rodriguez, M. A.; Schorr, N. B.; Wygant, B. R.; Okasinski, J. S.; Chuang, A. C.; Lambert, T. N.; Gallaway, J. W. Li-Ion and Na-Ion Intercalation in Layered MnO2 Cathodes Enabled by Using Bismuth as a Cation Pillar. *J. Mater. Chem. A* **2023**, *11* (21), 11272–11287. https://doi.org/10.1039/D3TA00684K.

(30) Wang, C.; Liu, L.; Zhao, S.; Liu, Y.; Yang, Y.; Yu, H.; Lee, S.; Lee, G.-H.; Kang, Y.-M.; Liu, R.; Li, F.; Chen, J. Tuning Local Chemistry of P2 Layered-Oxide Cathode for High Energy and Long Cycles of Sodium-Ion Battery. *Nat Commun* **2021**, *12* (1), 2256. https://doi.org/10.1038/s41467-021-22523-3.

(31) Jing, Yikang, Wang, Haonan, Pacileo, Anthony T. ,. Strong, Nathanael, Qiao, Linna, Zhou, Guangwen; Liu, H. Ca Pillar Effect on the Electrochemistry and Stability of P2-Na_xCa_yFe_0.5Mn_0.5O_2 for Sodium-Ion Batteries. *Phys. Rev. Mater.* **2025**. https://doi.org/10.1103/t868-pv1p.

(32) Han, S. C.; Lim, H.; Jeong, J.; Ahn, D.; Park, W. B.; Sohn, K.-S.; Pyo, M. Ca-Doped NaxCoO2 for Improved Cyclability in Sodium Ion Batteries. *Journal of Power Sources* **2015**, *277*, 9–16. https://doi.org/10.1016/j.jpowsour.2014.11.150.

(33) Nayak, D.; Jha, P. K.; Ghosh, S.; Adyam, V. Aluminium Substituted β–Type NaMn1-xAlxO2: A Stable and Enhanced Electrochemical Kinetic Sodium-Ion Battery Cathode. *Journal of Power Sources* **2019**, *438*, 227025. https://doi.org/10.1016/j.jpowsour.2019.227025.

(34) Mendiboure, A.; Delmas, C.; Hagenmuller, P. Electrochemical Intercalation and Deintercalation of NaxMnO2 Bronzes. *Journal of Solid State Chemistry* **1985**, *57* (3), 323–331. https://doi.org/10.1016/0022-4596(85)90194-X.

(35) Parant, J.-P.; Olazcuaga, R.; Devalette, M.; Fouassier, C.; Hagenmuller, P. Sur quelques nouvelles phases de formule NaxMnO2 ($x \leqslant 1$). *Journal of Solid State Chemistry* **1971**, *3* (1), 1–11. https://doi.org/10.1016/0022-4596(71)90001-6.

(36) Han, M. H.; Gonzalo, E.; Singh, G.; Rojo, T. A Comprehensive Review of Sodium Layered Oxides: Powerful Cathodes for Na-Ion Batteries. *Energy Environ. Sci.* **2014**, *8* (1), 81–102. https://doi.org/10.1039/C4EE03192J.

(37) Kubota, K.; Kumakura, S.; Yoda, Y.; Kuroki, K.; Komaba, S. Electrochemistry and Solid-State Chemistry of NaMeO2 (Me = 3d Transition Metals). *Advanced Energy Materials* **2018**, *8* (17), 1703415. https://doi.org/10.1002/aenm.201703415.

(38) Kumakura, S.; Tahara, Y.; Kubota, K.; Chihara, K.; Komaba, S. Sodium and Manganese Stoichiometry of P2-Type $Na_{2/3}$ MnO_2. *Angew Chem Int Ed* **2016**, *55* (41), 12760–12763. https://doi.org/10.1002/anie.201606415.

(39) Manzi, J.; Paolone, A.; Palumbo, O.; Corona, D.; Massaro, A.; Cavaliere, R.; Muñoz-García, A. B.; Trequattrini, F.; Pavone, M.; Brutti, S. Monoclinic and Orthorhombic NaMnO2 for Secondary Batteries: A Comparative Study. *Energies* **2021**, *14* (5), 1230. https://doi.org/10.3390/en14051230.

(40) Delmas, C.; Fouassier, C.; Hagenmuller, P. Structural Classification and Properties of the Layered Oxides. *Physica B+C* **1980**, *99* (1), 81–85. https://doi.org/10.1016/0378-4363(80)90214-4.

(41) Shibata, T.; Kobayashi, W.; Moritomo, Y. Sodium Ion Diffusion in Layered NaxMnO2 ($0.49 \leq x \leq 0.75$): Comparison with NaxCoO2. *Appl. Phys. Express* **2014**, *7* (6), 067101. https://doi.org/10.7567/APEX.7.067101.

(42) Ugata, Y.; Motoki, C.; Dokko, K.; Yabuuchi, N. Fundamental Methods of Electrochemical Characterization of Li Insertion Materials for Battery Researchers. *J Solid State Electrochem* **2024**, *28* (3), 1387–1401. https://doi.org/10.1007/s10008-023-05670-z.

(43) Wood, M.; Gao, X.; Shi, R.; Heo, T. W.; Espitia, J. A.; Duoss, E. B.; Wood, B. C.; Ye, J. Exploring the Relationship between Solvent-Assisted Ball Milling, Particle Size, and Sintering Temperature in Garnet-Type Solid Electrolytes. *Journal of Power Sources* **2021**, *484*, 229252. https://doi.org/10.1016/j.jpowsour.2020.229252.

(44) Dolla, T. H.; Ajayi, S. O.; Sikeyi, L. L.; Mathe, M. K.; Palaniyandy, N. Advances in Solid-State Batteries Fabrication Strategies for Their Manufacture. *Journal of Energy Storage* **2025**, *106*, 114737. https://doi.org/10.1016/j.est.2024.114737.

(45) Cushing, B. L.; Wiley, J. B. Topotactic Routes to Layered Calcium Cobalt Oxides. *Journal of Solid State Chemistry* **1998**, *141* (2), 385–391. https://doi.org/10.1006/jssc.1998.7957.

(46) An, S.; Karger, L.; Müller, P.; Lin, J.; Vasala, S.; Baran, V.; Dreyer, S. L.; Zhang, R.; Ulusoy, F.; Kondrakov, A.; Janek, J.; Brezesinski, T. Exploring Calcium Pillaring of O3-Type NaNi0.9Ti0.1O2 Cathodes to Advance Na-Ion Battery Technology. *Chemical Engineering Journal* **2025**, *509*, 160939. https://doi.org/10.1016/j.cej.2025.160939.

(47) Diffusional Transformations. In *Pergamon Materials Series*; Elsevier, 2007; Vol. 12, pp 555–716. https://doi.org/10.1016/S1470-1804(07)80060-5.

(48) *Miscibility Gap - an overview | ScienceDirect Topics*. https://www-sciencedirect-com.proxy.binghamton.edu/topics/engineering/miscibility-gap (accessed 2025-11-11).

(49) Zheng, L.; Bennett, J. C.; Obrovac, M. N. Stabilizing NaCrO2 by Sodium Site Doping with Calcium. *J. Electrochem. Soc.* **2019**, *166* (10), A2058. https://doi.org/10.1149/2.1041910jes.

(50) Zhu, W.; Liu, D.; Paolella, A.; Gagnon, C.; Gariépy, V.; Vijh, A.; Zaghib, K. Application of Operando X-Ray Diffraction and Raman Spectroscopies in Elucidating the Behavior of Cathode in Lithium-Ion Batteries. *Front. Energy Res.* **2018**, *6*. https://doi.org/10.3389/fenrg.2018.00066.

(51) P. Black, A.; Sorrentino, A.; Fauth, F.; Yousef, I.; Simonelli, L.; Frontera, C.; Ponrouch, A.; Tonti, D.; Rosa Palacín, M. Synchrotron Radiation Based Operando Characterization of Battery Materials.

Chemical Science **2023**, *14* (7), 1641–1665. https://doi.org/10.1039/D2SC04397A.

(52) Hess, M.; Sasaki, T.; Villevieille, C.; Novák, P. Combined Operando X-Ray Diffraction–Electrochemical Impedance Spectroscopy Detecting Solid Solution Reactions of LiFePO4 in Batteries. *Nat Commun* **2015**, *6* (1), 8169. https://doi.org/10.1038/ncomms9169.

(53) Marschilok, A. C.; Bruck, A. M.; Abraham, A.; Stackhouse, C. A.; Takeuchi, K. J.; Takeuchi, E. S.; Croft, M.; Gallaway, J. W. Energy Dispersive X-Ray Diffraction (EDXRD) for Operando Materials Characterization within Batteries. *Phys Chem Chem Phys* **2020**, *22* (37), 20972–20989. https://doi.org/10.1039/d0cp00778a.

(54) Yin, J.-W.; Wu, Y.-M.; Liu, X.-Y.; Li, J.; Wang, P.-F.; Liu, Z.-L.; Wang, L.-L.; Shu, J.; Yi, T.-F. Insights into Degradation Mechanisms and Engineering Strategies of Layered Manganese-Based Oxide Cathodes for Sodium-Ion Battery. *Green Energy & Environment* **2025**. https://doi.org/10.1016/j.gee.2025.07.013.

(55) Zhang, L.; Deshmukh, J.; Hijazi, H.; Ye, Z.; Johnson, M. B.; George, A.; Dahn, J. R.; Metzger, M. Impact of Calcium on Air Stability of Na[Ni1/3Fe1/3Mn1/3]O2 Positive Electrode Material for Sodium-Ion Batteries. *J. Electrochem. Soc.* **2023**, *170* (7), 070514. https://doi.org/10.1149/1945-7111/ace55a.